An Investigation on the Plane-Strain Fracture Toughness of a Water Atomized 4130 Low-Alloy Steel Processed by Laser Powder Bed Fusion

M. Abdelwahed[a, b, *], S. Bengtsson[c], M. Boniardi[a], A. Casaroli[a], R. Casati[a], M. Vedani[a]

An Investigation on the Plane-Strain Fracture Toughness of a Water Atomized 4130 Low-Alloy Steel Processed by Laser Powder Bed Fusion

M. Abdelwahed[a, b, *], S. Bengtsson[c], M. Boniardi[a], A. Casaroli[a], R. Casati[a], M. Vedani[a]

[a]Department of Mechanical Engineering, Politecnico di Milano, Milan, Italy.
[b]Department of Design and Production Engineering, Faculty of Engineering, Ain Shams University, Cairo, Egypt.
[c]Höganäs AB, Höganäs, Sweden.

Abstract

A water atomized 4130 steel powder was processed by Laser powder bed fusion and investigated both in the as built condition and after the quench and tempering heat treatment. Analyses were focused on the different microstructures developed and on steel fracture behaviour in terms of tensile fracture elongation, Charpy impact properties and linear elastic fracture toughness. Comparisons were also drawn by testing a reference 4130 steel produced using gas atomized powders. The slightly higher oxygen content found in the water atomized powders led to the formation of finely dispersed nano-size oxide particles in the steel matrix. It was found that these nano-sized inclusions have a minor effect on the tensile properties, but a significant influence on the impact toughness response. The fracture toughness tests showed that the orientation leading to propagation of cracks along the inter-layer planes represented the most critical situation, and the steel toughness could be significantly improved after the quench and tempering treatment owing to the achievement of a fully martensitic and more homogeneous microstructure.

The results suggest that the investigated water atomized low-alloy steel powder feedstock can be considered as a suitable and cheaper alternative for structural parts produced by additive manufacturing, which could replace the more popular gas atomized steel grades.

Keywords

Laser Powder Bed Fusion; Water Atomized Powder; Low-Alloy Steel; Non-metallic Inclusions; Hardenability; Fracture Toughness.

1. Introduction

The laser powder bed fusion (L-PBF) technology has been well recognized among the different manufacturing processes due to the remarkable ability of facilitating the production of complex-shaped metallic components with outstanding mechanical properties for light-weight applications. Though, the commercially available steels for L-PBF are still limited to stainless steels, maraging grades, and few other tool steels [1]. Recently, the interest on low-alloy steels for L-PBF gained an increasing interest owing to their low-cost and favorable properties for structural applications [2–11].

The expected low cost of these steels not only derives from the lower amount of alloy elements, but it could stem from the adoption of cheaper powder production routes such as water atomization (WA). Indeed, WA is a popular process which provides cost-effective feedstocks for several powder metallurgy applications, especially in large batches for mass-production of components [20,21]. It is to consider that the nature of the atomization process, which uses water jets to atomize the steel melt, contributes to increase the oxygen level in the powder, and to the formation of micrometer- and sub-micrometer oxide-based inclusion in the steel matrix after L-PBF [9,22]. According to a previous study, the L-PBF of WA 4130 alloy could deliver outstanding tensile properties, even after various powder recycling events, though a slight reduction in strength and ductility could be measured when compared to a counterpart steel fabricated by GA powder with similar chemical composition [23].

Several efforts have been made to identify the role of alloying elements, the as-built (AB) microstructure and effects of thermal treatments on the properties of low-alloy steel grades, even if obtained from gas atomized (GA) powders, which represent the reference processing route for LPBF powders. A first investigation was carried out on a 24CrNiMo steel highlighting the heterogeneous and spatial-dependent microstructure generated by the different local thermal cycles experienced along the build height [12]. Directional-dependent tensile properties were also recorded in most of the L-PBF processed steels, which could be reduced by producing a more homogenous microstructure through a post-process thermal treatment of quench and tempering (Q&T) [3,4,10,13]. The investigated low-alloy steels showed high tensile properties, over those of the corresponding wrought alloys. However, the knowledge on other mechanical properties such as the impact and fracture toughness still needs to be improved in order to gain a greater confidence level on low-alloy steels processed by L-PBF for structural applications. In this respect, Wang and co-authors [5] tested the impact toughness of a 30CrMnSi alloy after L-PBF, and also proposed few thermal treatments to enhance their performance. The AB steel was able to absorb 11.4 J that is equivalent to almost 25% of the corresponding forged and annealed counterpart, due to the dissimilarity in microstructures. It was confirmed that the tempering temperature of a quenched microstructure had a significant effect on the toughness values, since the tempering treatments performed at 550 ^{o}C and 650 ^{o}C led to impact energies of 12.4 J and 29.1 J, respectively. On the contrary, in an investigation carried out on a 30CrNiMo8 grade [10], the authors reported impact toughness values of around 100 J in both AB and Q&T conditions. It is noteworthy to mention that these energy values are significantly higher than those generally achieved by the wrought alloy. Hence, it becomes clear that a general trend on the fracture behavior of L-PBF processed steels cannot be estimated yet, and further investigations on the toughness of low-alloy steels produced by L-PBF are necessary for their adoption in structural applications.

Fracture toughness is a significant material property that describes the structural integrity and reliability of materials, considering the combined effect of an applied load in presence of defects [14]. In L-PBF of ferrous alloys, the main factors affecting fracture toughness are directly associated to microstructure, process-related defects, residual stresses, and steel cleanliness. Suryawanshi et. al. [15] reported that the K_{IC} value of a L-PBF processed 316L steel ranges between 63 and 87 MPa√m, which is much lower compared to the same alloy in wrought form (112 to 278 MPa√m). It was claimed that this drop is mainly due to reduced ductility, presence of defects, lack of transformation-induced plasticity effect in the L-PBF alloy. The authors also investigated the anisotropy in properties and showed that the fracture toughness is slightly higher when the cracks grew orthogonally to the building direction. Conversely, the K_{IC} value of a L-PBF 18Ni300 maraging steel grade after aging was found to be 70 – 75 MPa√m, which is comparable to the wrought alloy despite the dissimilarity in the microstructures [16].

It is well known that also the presence of non-metallic inclusions in steels affects ductility and toughness. Several investigations have been carried out to understand the effect of sulfide-based inclusions on the fracture toughness of steels [17,18]. It was found that the sulfides act as crack initiators and reduce the K_{IC} value by 25 – 50%. Oxide-based inclusions are more likely to be found in L-PBF processed steels, since the feedstock powder already contains limited amounts of oxygen from the atomization process itself [9], as a result of contamination during powder handling and storage, or due to the oxygen pickup from the chamber environment during the L-PBF process. Lou and co-workers [19] reported that oxide-based inclusions stimulate an early initiation of micro-voids that dramatically affects the toughness of L-PBF 316L stainless steel compared to the wrought alloy.

The scope of this investigation is therefore primarily oriented towards a better understanding of the properties of a WA 4130-steel processed by L-PBF. The microstructures developed after L-PBF and Q&T treatments, hardness and tensile properties as well as plane strain fracture toughness of the WA steel was especially studied considering the different orientations with respect to the building direction. Moreover, the contribution of oxide inclusions on the impact toughness response was evaluated by comparing the WA powder with a standard GA powder of the same alloy.

2. Material and Experimental Procedures

A water atomized 4130 low-alloy steel powder was mainly used for the present investigation, whereas a reference 4130 steel obtained by GA powders was also considered for selected comparative tests. Accordingly, the steels were labelled as W-4130 and G-4130, respectively. The G-powder had a spherical morphology with particle size distribution characterized by …., while the W-powder consisted of irregular-shaped particles featuring a size of …….. As expected, the W-type powder showed a relatively lower flowability compared to the gas atomized powder, Further powder characteristics have been provided in a previous paper [13].

An open L-PBF system featuring flexible control over the laser system and optical chain (LLA150R, 3DNT) was adopted to process the steel powders under an Argon-shielding atmosphere, in which the oxygen level was kept below 2500 ppm. A single mode fiber-laser of 190 W was applied on a powder layer of 40 μm in thickness to process the specimens. Based on a preliminary optimization of parameters, the hatching distance was set to 90 μm, while the laser scanning velocity was defined to 650 mm/s and 500 mm/s for the G-4130 and the W-4130 powders, respectively. Moreover, a stripe scanning strategy was used with an incremental rotation angle of 67^{o} for each deposited layer.

Chemical analyses were performed by a Bruker Q4 TASMAN equipment to measure the composition of the steel specimens after L-PBF. Microstructural investigations were performed on the processed specimens directly after polishing down to 50 nm colloidal silica and etching. Nital reagent was generally used as etchant to reveal the microstructure whereas Picral was preferred to highlight the melt pool boundaries. The microstructure was characterized by a Nikon Eclipse LV150NL optical microscope, and a Zeiss Sigma 500 VP field-emission scanning electron microscope equipped with energy-dispersive X-ray spectroscopy. Further characterization was carried out by electron backscattered diffraction (EBSD) operating with an accelerating voltage of 20 KV and a step size resolution of 0.35 μm.
Thermodynamic simulations to support phase identification were conducted with ThermoCalc AB software relying on the TCFE9 Steels/Fe-alloys database.

Jominy specimens of 27 mm in diameter and 103 mm in length were fabricated by L-PBF and machined to a final standard size in order to measure the hardenability of both steels. The mechanical properties of the steels were evaluated by tensile testing, impact toughness, and plane-strain fracture toughness tests. Sub-sized cylindrical dog-bone specimens were extracted from bars fabricated orthogonally to the building direction and tested according to ASTM E8M standard. Charpy V-notch specimens were machined from 2 mm-oversized bars oriented in the same direction. EN ISO 148-1 standard procedures were followed to determine the impact toughness at room temperature.

Oversized coupons (41 mm x 39 mm x 18 mm) for the fracture toughness tests were fabricated from the WA feedstock considering two orientations, where the crack propagation plane was parallel (L-S) or orthogonal (S-L) to the building direction, as displayed in Fig. 1. The specimens were tested either in AB state or after water quenching from 840 ºC and tempering at 550 ºC for 1 hour (Q&T). Afterwards, the coupons were machined to obtain compact tension (CT) fracture toughness specimens, according to ASTM E1820 standard with step notches to measure the crack opening displacement (COD) by a clip-on extensometer. Side groves were also machined to ensure a crack-front flatness and to provide reliable measurements of the crack length. Fatigue pre-cracking and fracture testing campaign were conducted by using a servo-hydraulic machine (type MTS 810). After performing the tests, specimens were oxidized in a muffle furnace, immersed in liquid nitrogen and broken in a brittle manner. The standard was followed to assess the initial and the final crack length, using nine equally-spaced positions to determine the average initial crack size. All tests were carried out at room temperature, using at least three specimens for each condition. The fracture surfaces of specimens were analysed by a Zeiss SteREO Discovery v12 stereoscope as well as a Zeiss EVO-50XVP SEM to define the failure mechanisms.

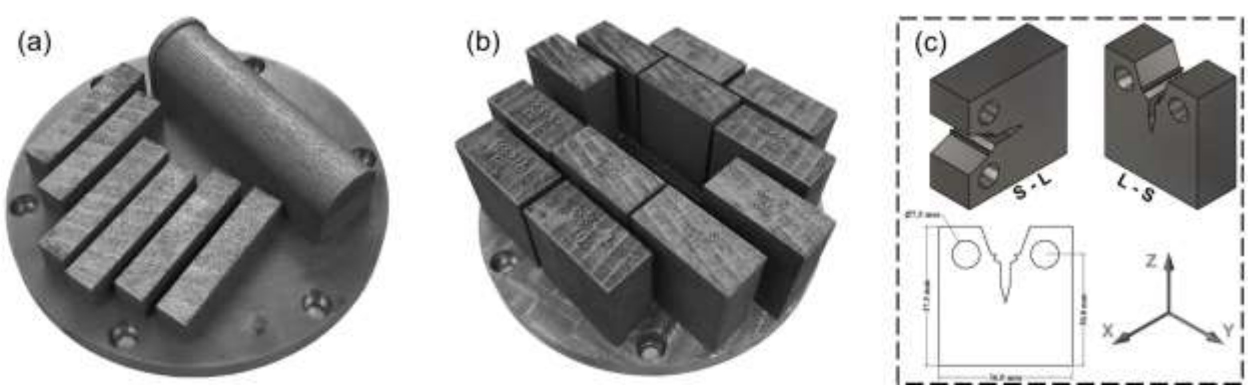

Fig. 1: views of the fabricated (a) Jominy and Charpy specimens, (b) fracture toughness coupon blocks, and (c) a schematic representation of the orientation of the fracture toughness specimens. The z-axis corresponds to building direction, normal to baseplate plane (x-y)

3. Results and Discussion

3.1. Chemical composition after L-PBF

The chemical composition of the investigated steels after L-PBF is given in Table 1. A lower carbon content is measured for the L-PBF W-4130 steel compared to the gas atomized counterpart. This could be due to variability of elemental composition during feedstock preparation and partially to loss of carbon during L-PBF processing. It has been reported that the laser processing of GA low-alloy steel powders is generally associated with a reduction in carbon content between 5% and 12% in the AB components, regardless the differences in composition and processing conditions [11,12,24,25]. A similar amount of 6% loss in carbon was also measured for a L-PBF steel processed from a WA powder with 0.33 wt.% C [26].

Table 1. Chemical analysis of the L-PBF processed steels.

Alloy	**Chemical Composition (wt. %)**						
	C	Cr	Mo	Si	Mn	Ni	O*
G-4130	0.317 ± 0.005	1.182 ± 0.006	0.152 ± 0.005	0.271 ± 0.008	0.694 ± 0.003	0.144 ± 0.009	0.05
W-4130	0.234 ± 0.004	1.330 ± 0.005	0.285 ± 0.007	0.629 ± 0.017	0.050 ± 0.000	0.090 ± 0.004	0.29

*Amount of oxygen was measured on the starting feedstock powders.

The reduced amount of carbon in the as-built W-4130 specimens could be partially related to the higher oxygen level in the starting powder, which stimulate the formation of CO gas during the melting stages. Thermodynamic simulations were performed on a simplified Fe-0.3C system with various oxygen contents to better quantify this effect. The results are displayed in Fig. 2 and indicate that higher contents of oxygen contribute to a pronounced increase in the fraction of CO above the liquidus temperature. Therefore, it could be assumed that the oxygen content in the starting powder plays the significant role on the carbon loss during L-PBF of steels.

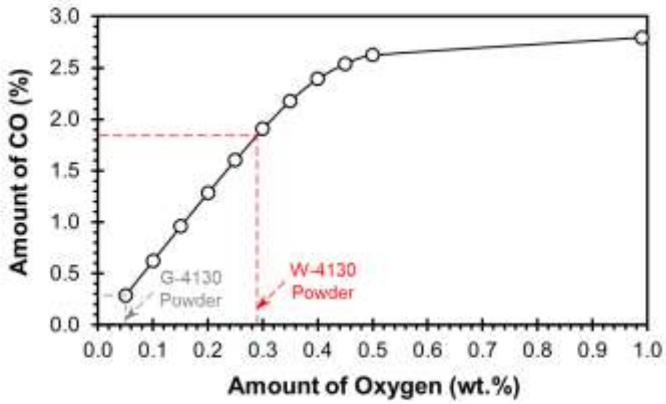

Fig. 2: Mole fraction of CO gas above 1600 ºC as a function of oxygen content in a Fe-0.3C system (computed under equilibrium hypothesis).

3.2. Hardenability of the L-PBF 4130 Steels

Given the differences in composition (especially for C and Mn) of the two investigated steels, their hardenability was experimentally measured in order to improve the understanding of the achievable properties. The results of the Jomini tests are summarized in Fig. 3. It is revealed that the hardness profile of the G-4130 steel follows the mean values also expected by a similar wrought alloy [27]. However, a significant reduction in the hardness values was measured for the W-4130 steel, indicating a lower hardenability. This effect is supposed to be related to the modified composition of the W-4130 powder, featuring lower C and lack of Mn. In addition, oxide-based inclusions, more frequent in the W-4130 version, could stimulate the nucleation of other constituents rather than martensite, hence play an important role on hardenability. Finally, the micrographs of Fig. 3(b) and 3(c) show the decarburized layer formed on surface of Jomini samples during the austenitizing step, prior to quenching. Based on microstructure observation, a ferrite layer of about 300 µm was formed on the surface of the W-4130 specimen, corresponding to almost 3 times that of the G-4130 steel. It is assumed that the lower starting value of C would ease the achievement of the ferritic field when the steels are held at high temperature in a furnace with oxidizing air environment, hence widening the ferritic layer in the W-4130 specimens.

Beyond the decarburized surface, a fully martensitic matrix up to 6 mm could be observed for the G-4130, while a mixture of martensite and other ferrite constituents could be detected for the WA alloy confirming the relatively lower hardenability after quenching.

m

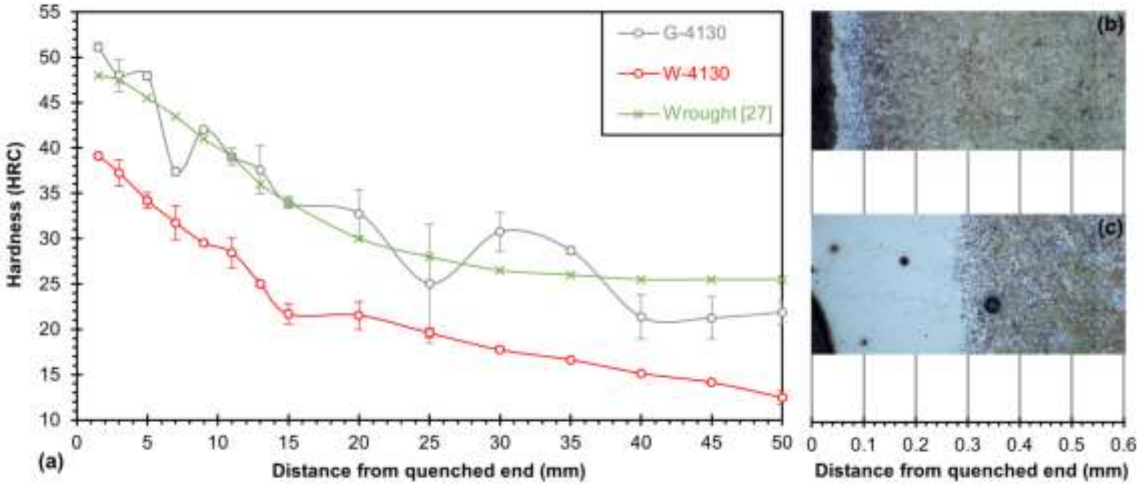

Fig. 3: (a) Hardenability curves of the investigated steels. The hardness values of a wrought 4130 steel [27] is also reported. Optical micrographs of sections portions of the Jominy specimens close to surface at the end quench location for (b) G-4130 and (c) W-4130 steel.

3.3. Microstructure Evolution

Fig. 4 depicts high magnification FE-SEM micrographs, highlighting the finely dispersed sub-micrometric oxide inclusions in the matrix of the investigated steels. The thermodynamic simulations estimated the formation of dual-phase oxides of type MnO-SiO_2 in the G-4130 steel, whereas mono-phase SiO_2 inclusions in the W-4130 alloy are expected. The elemental compositions measured by EDS point analyses confirmed the hypotheses by which the oxides found in the G-4130 steel were rich in Mn, Si, and O while those embedded in the matrix of the W-4130 steel were mainly formed by Si and O. Moreover, it could be observed that the fraction of oxides occupying the W-4130 matrix was about 0.5% while that observed in the G-4130 steel was lower than 0.1%.

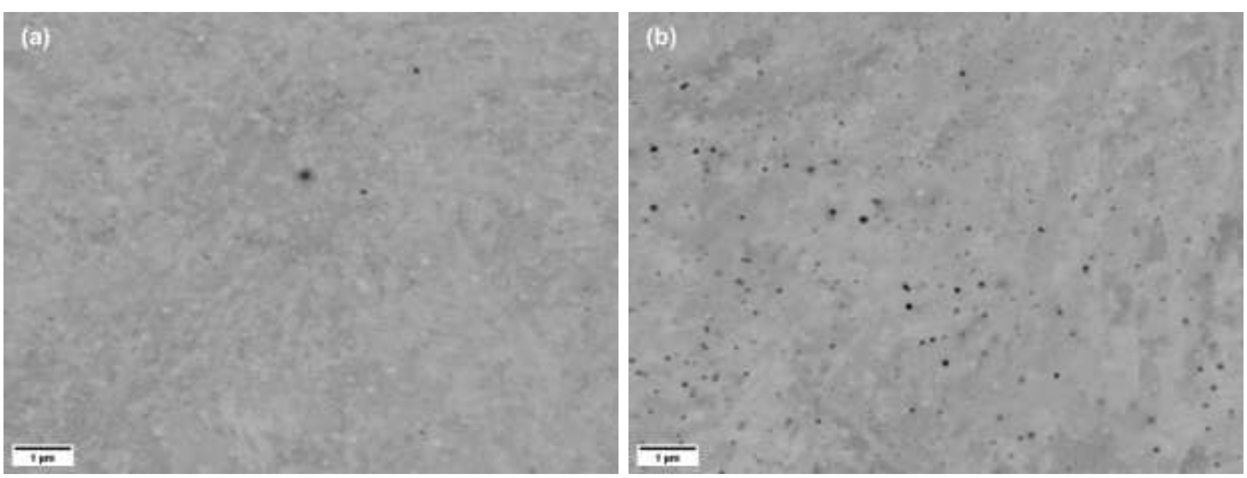

Fig. 4: FE-SEM micrographs showing the non-metallic inclusions in the (a) G-4130 and (b) W-4130 steels.

EBSD analyses results carried out on the investigated steels after L-PBF are collected in Fig. 5. In Fig. 5 (a) and 5(d) band contrast (BC) images are provided. The BC method has been widely used as an approach to differentiate between phases having similar crystal structure such as martensite, bainite, and ferrite [28,29]. This method is based on the diffraction pattern intensity during data acquisition in which the phase with higher lattice imperfections provides a lower pattern quality, corresponding to darker regions. From obtained results, it could be clearly observed that the melt pool boundaries in the steel are highlighted by relatively lower pattern intensities, indicating more imperfections located in those regions. In addition, finer microconstituents are found at the melt pool boundaries compared to other zones. This is presumably due to the relatively higher cooling rates that are experienced close the melt pool boundaries during solidification [30]. The inverse pole figures (IPFs) provided in Fig. 5(b) and 5(e) show highly misoriented microstructures and an epitaxial growth of the grains across several melt pools. Moreover, the Kernel average misorientation (KAM) analyses depicted in Fig. 5(c) and 5(f) indicate a nearly homogenous local strain distribution within the microstructures after L-PBF.

Finally, the analysis about grain boundary misorientation profiles provided in Fig 5(g) reveals a substantially comparable trend between the two investigated steels. The as-built microstructures are primarily separated by a high fraction of low angle grain boundaries denoting the dominant presence of sub-structures within the martensitic blocks. Furthermore, a second population of high-angle grain boundaries centered at about 60^{o} was detected. It has been demonstrated that a strong peak at this particular angle is usually detected for martensitic structures [31,32], which corresponds to the block boundaries [33].

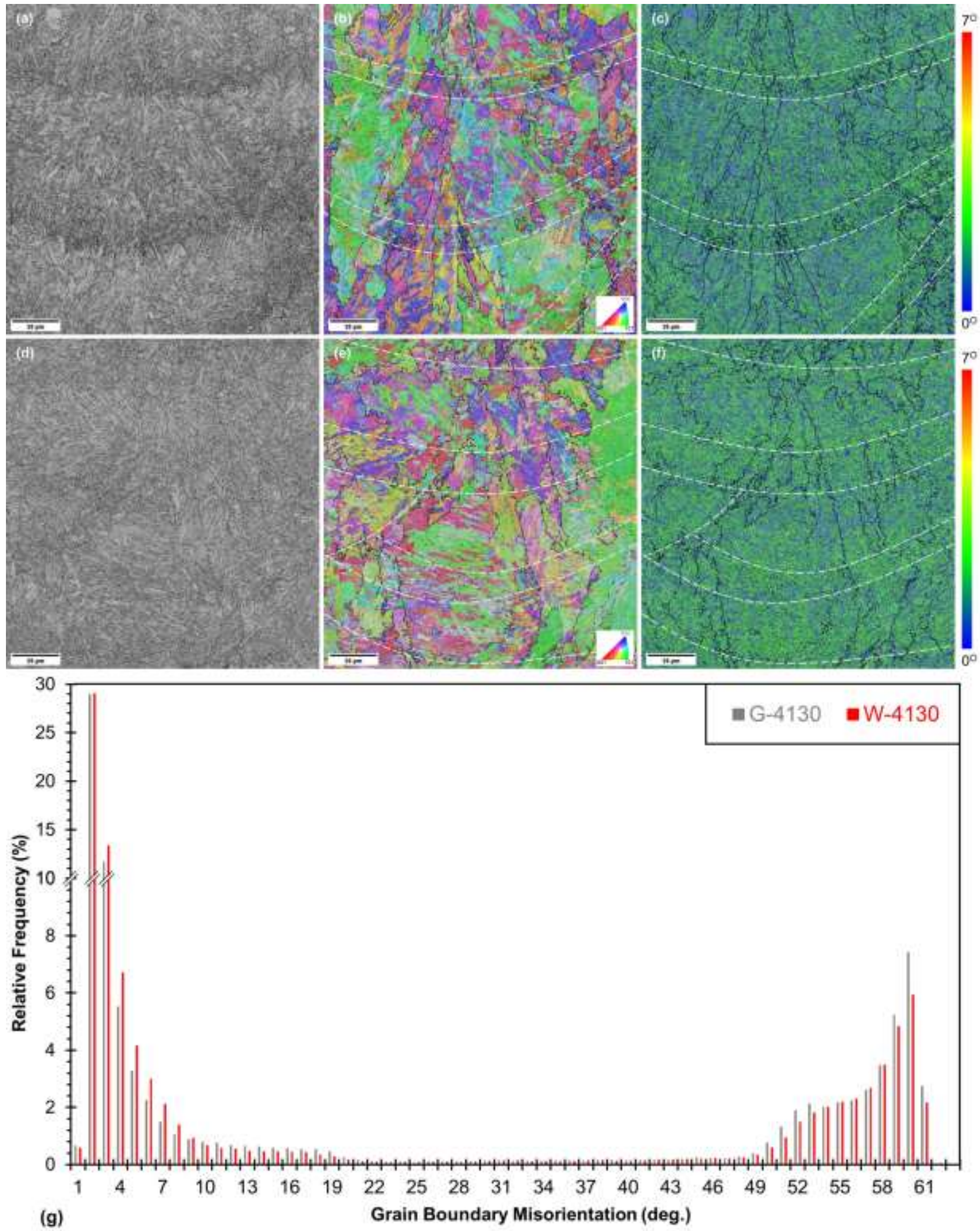

Fig. 5: EBSD measurements showing band contrast micrographs, IPF, and KAM maps, respectively, for (a-c) G-4130 and (d-f) W-4130 steels. (g) grain boundary misorientation profile for the investigated steels.

Fig. 6 displays high magnification FE-SEM micrographs of the investigated steels in both AB and Q&T conditions. During L-PBF, the progressive overlapping of layers and related heat dissipation generates a partial tempering effect on the rapidly cooled microstructure, which in turn leads to the precipitation of carbides [8,12]. Conversely, the conventional quenching and isothermal tempering resulted in fine dispersed secondary phase particles decorating the block and lath boundaries, as shown in Fig 6(b) and 6(d). According to the literature, such phases are assumed to be carbides mainly of the $M_{23}C_6$ type [23].

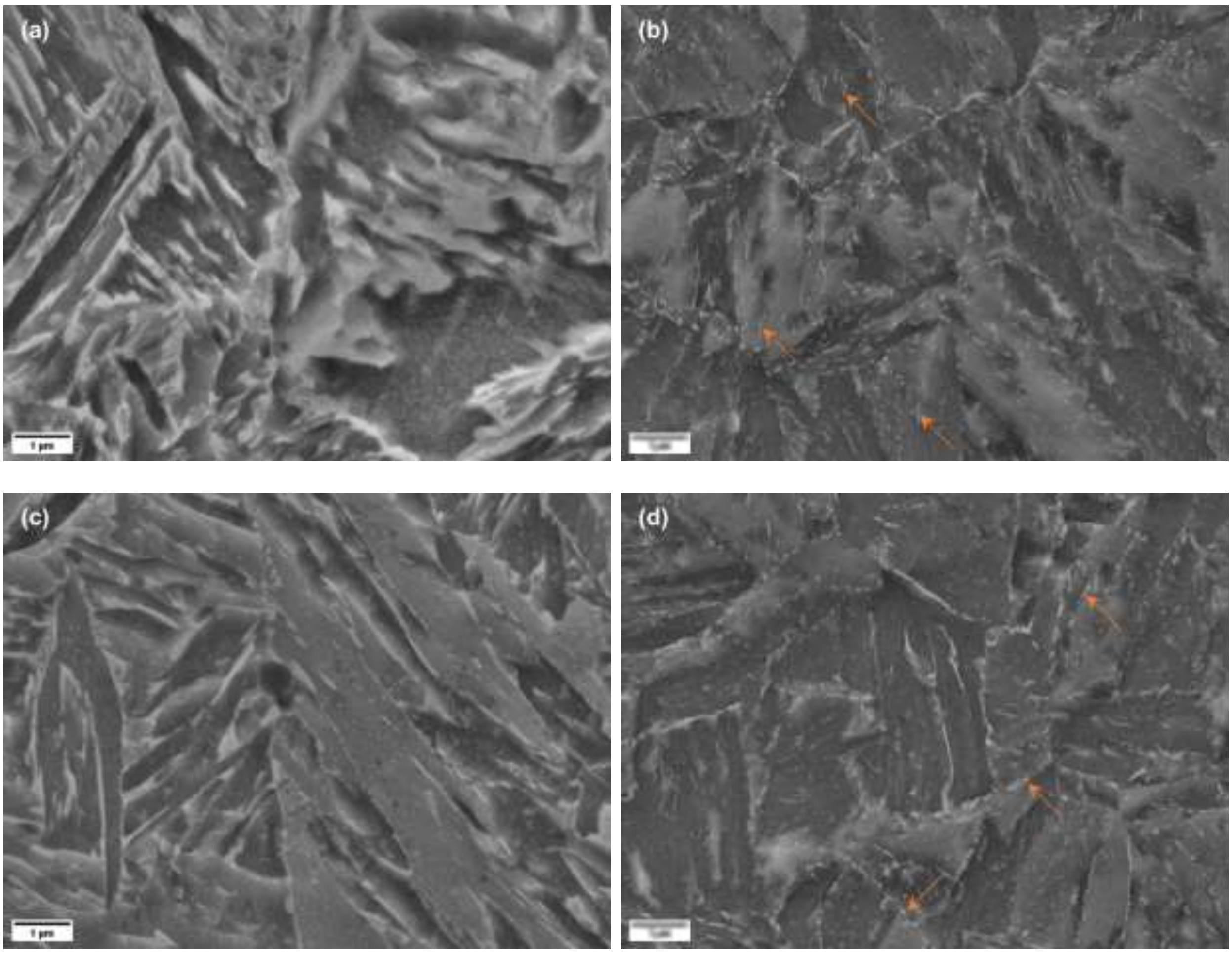

Fig 6: FE-SEM micrographs of G-4130 in (a) AB and (b) Q&T conditions, W-4130 in (c) AB and (d) Q&T conditions. (arrows refers to the precipitated carbides).

3.4. Mechanical Properties

3.4.1. Microhardness

Hardness profiles were measured across the thickness of the Charpy specimens to collect further information about the actual hardening achieved by the two steels either after rapid quenching from the L-PBF process (AB condition) or after the conventional Q&T treatment. The results are displayed in Fig. 7. Both steels in AB condition showed fluctuations in the microhardness values owing to the heterogeneous microstructure encountered when crossing the partially overlapped melt pools (see description in section 3.3). According to the lower C content and the reduced hardenability measured for the W-4130 steel, the average hardness level achieved (398 ± 18 $HV_{0.5}$) was lower than that of the G-4130 version (459 ± 23 $HV_{0.5}$) in AB condition. On the contrary, after Q&T treatment, the investigated steels provided a more homogeneous microstructure and reached similar hardness values, of 379 ± 9 $HV_{0.5}$ and 363 ± 9 $HV_{0.5}$, for the W-4130 and G-4130 steels, respectively. It is to remark that both alloys did not show any drop in hardness towards the center of specimen thickness, suggesting an acceptable hardenability within the 12- thickness sample volume.

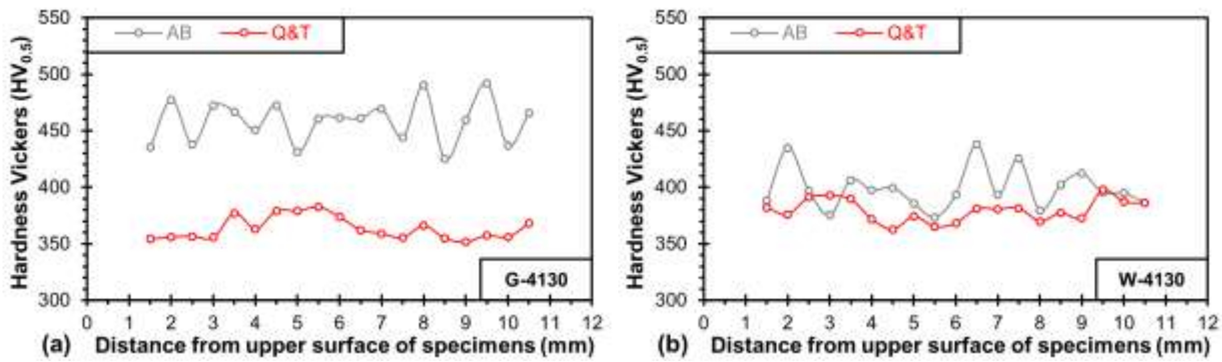

Fig. 7: Microhardness profiles of the investigated (a) G-4130 and (b) W-4130 steels.

3.4.2. Tensile Behavior

The tensile curves recorded from the W-4130 steel in AB and Q&T conditions are displayed in Fig. 8. The curves show an almost flat plastic plateau for the heat-treated steel after the linear elastic stage, while a more evident strain hardening response was detected in AB condition. Moreover, the acquired results showed that the steel in AB condition was able to deliver the highest offset yield and ultimate tensile strength, of 1068 ± 6 MPa and 1160 ± 2 MPa, respectively. Comparably, the Q&T steel provided a yield strength of 1070 ± 0 MPa and tensile strength of 1126 ± 2 MPa with a significant improvement in the fracture elongation from 5.00 ± 0.10 % to 7.05 ± 0.15 %, which is supposed to be promoted by the more homogenously tempered microstructure generated after the post-process thermal treatment.

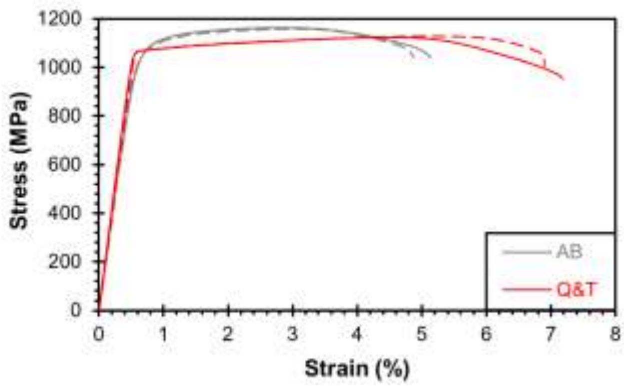

Fig. 8: Tensile curves of the investigated W-4130 steel (dashed-lines correspond to the replicated results).

3.4.3. Impact Toughness

The energy absorbed during the impact tests of both steels are summarized in Table 2. It can be observed that the Q&T treatment enhances the impact toughness of the G-type steels with respect to the AB condition, though the measured values are still lower than those expected by the standard 4130 wrought steel [27]. Conversely, in the WA steel, the Q&T treatment did not provide any substantial improvement in toughness with respect to AB condition. From a direct comparison between the two steels variants, it is readily seen that the W-4130 steel shows lower toughness properties in both investigated conditions. This behaviour is supposed to be related to the larger presence of oxide-based inclusions, that could assist crack initiation and growth. A similar behaviour was also reported by Salandre et. al. [34] who investigated an L40 tool steel which provided an impact toughness of 50 J when using gas atomized powders, that significantly dropped to 13 J using water atomized powders of the same steel grade.

Table 2. Impact energy of the investigated low-alloy steels along with available data from the literature for similar grades.

Steel Grade	Condition	Impact Energy (J)
G-4130	AB	18.9 ± 3.1
	Q&T-550 ºC	25.3 ± 2.4
W-4130	AB	12.3 ± 0.5
	Q&T-550 ºC	13.3 ± 0.5
30CrMnSi [5]	AB	11.4 ± 0.5
	Q&T-550 ºC	12.4 ± 0.6
	Q&T-650 ºC	29.1 ± 1.0
30CrNiMo8 [10]	AB	87.8 ± 11.9
	Q&T-560 ºC	108.8 ± 2.3

4340 [4]	Q&T-190 ºC	16.4 ± 1.7

Fig. 9(a) and 9(b) display representative stereo-microscope images of Charpy fracture surfaces of the G-4130 and the W-4130 alloys, respectively, in Q&T condition. A slightly higher area fraction occupied by lateral shear lips could be observed for the surfaces of the G-4130 steel, in agreement with its more ductile behaviour. A similar trend was also observed for the same steels in AB condition. The higher magnification SEM micrographs given in Fig 10, generally reveal the presence of fine dimples covering most of the fracture surfaces of both steels in both investigated tempers, indicating a microscopically ductile fracture mechanism taking place during the impact test. A few quasi-cleavage flat surfaces were additionally observed (more frequent in the Q&T alloys), as highlighted by the yellow arrows in Fig. 10(b) and 10(d). The relatively large craters observed in Fig. 10(d) refer to micro-porosities, presumably generated during the laser process by entrapped or released gases. It is to remark that few typical L-PBF lack of fusion defects were also occasionally detected on the fracture surfaces.

The most significant difference between the surfaces of the two investigated steels mainly consists of a wider population of spherical oxide-based inclusions found in micro- and submicrometer dimples (compare Fig 10(a) and Fig. 10(c))of the W-4130 steel samples, that are believed to rule the different impact toughness response of the investigated steels.

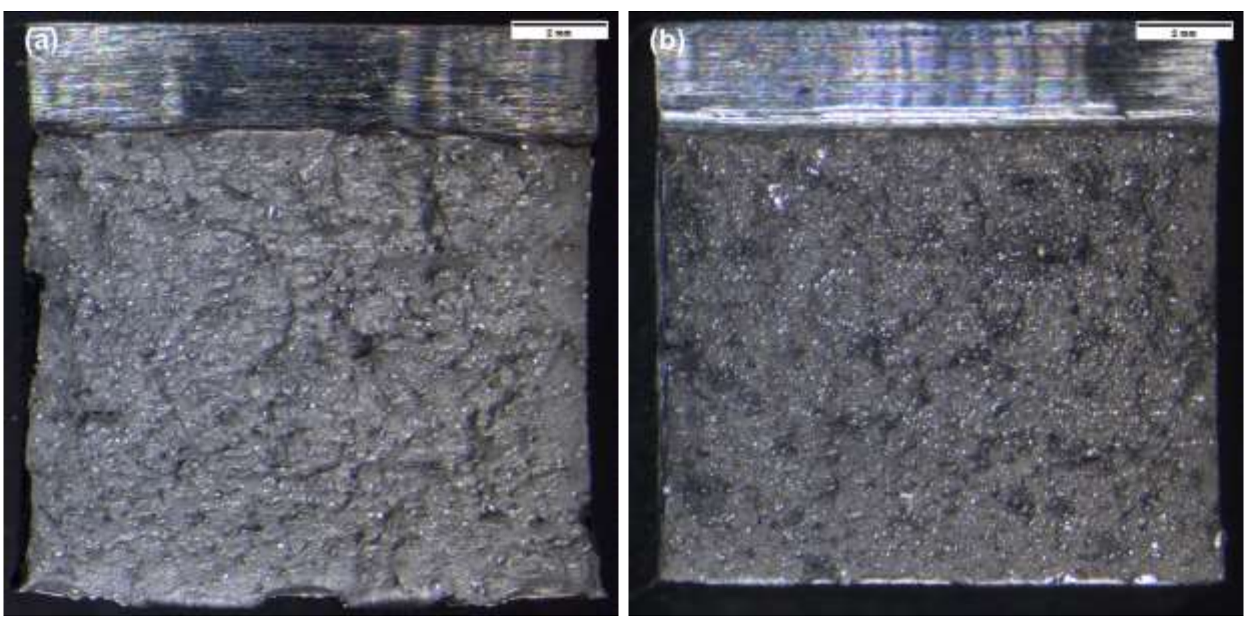

Fig. 9: Stereographic images of the fracture surface after Charpy impact tests of the (a) G-4130 and (b) W-4130 steels, both in Q&T condition.

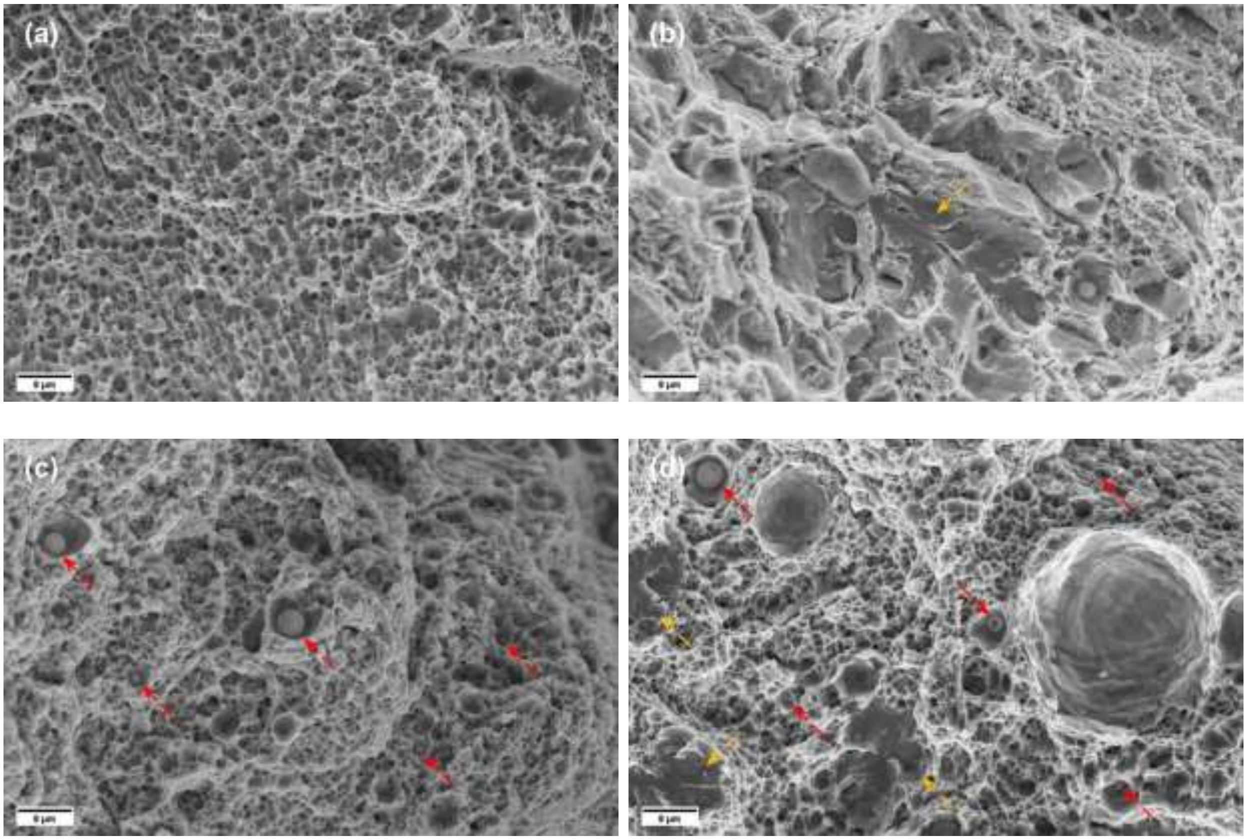

Fig. 10: SEM fractographs of the G-4130 steel in (a) AB and (b) Q&T condition, W-4130 steel in (c) AB and (d) Q&T condition. (yellow and red arrows refer to quasi-cleavage planes and oxide-based inclusions, respectively).

3.4.4. Fracture Toughness

Typical curves of the load vs. COD of the W-4130 steel in different conditions are provided in Fig.11(a), while a stereomicrograph of a fractured CT specimen showing the different zones of the crack development is given in Fig. 11(b). An elastic-plastic deformation behavior was observed for the WA steel in both conditions investigated and an anisotropic response was measured along the different loading orientations. The obtained J_{IC} values and the calculated K_{JIC} data are summarized in Table 3. It is observed that the crack propagation in a plane orthogonal to the building direction is the most critical situation in the L-PBF W-4130 steel. It is also found that the Q&T treatment is able to reduce the anisotropy and to improve the material toughness. Additionally, it is worth mentioning that the performance of the Q&T W-4130 alloy was found to be comparable with that of similar low-alloy steel grade processed from a GA powder, as reported in Table 3.

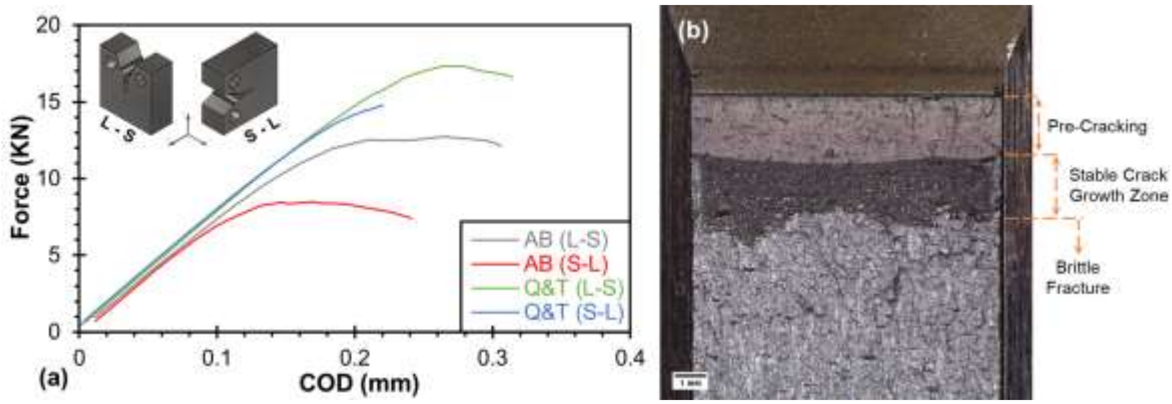

Fig. 11: Load vs. COD curves (a) of the W-4130 steel tested in different conditions and (b) typical CT fracture toughness specimens after fracture.

Table 3. Plane-strain fracture toughness values of the L-PBF processed W-4130 steel in different conditions.

Alloy	**Condition**	**Orientation**	**$J_{IC\text{-effective}}$ (KJ/mm^2)**	**K_{JIC} (MPa$\sqrt{m}$)**
W-4130	AB	L-S	14.3 ± 1.9	56.0 ± 3.8
		S-L	5.70 ± 0.6	35.5 ± 1.8
	Q&T	L-S	25.1 ± 0.2	74.3 ± 0.3
		S-L	15.6 ± 3.8	58.0 ± 7.5
4340 [4]	Q&T	L-S	-	54.3
		S-L	-	52.9

Fig. 12 displays the analyses performed on a cross section of a S-L W-4130 specimen tested in as built condition, when considering a region corresponding to the stable crack growth. Fractographs collected from the region corresponding to stable crack growth of the tested CT specimens of the W-4130 steel are depicted in Fig. 13. SiO_2 inclusion were again observed on the fracture surfaces along with few microporosities. A dimple rupture was detected for both investigated conditions and specimen orientation, highlighting the plastic deformation which took place during testing and the intrinsically ductile failure mechanism in the stable crack growth zone.

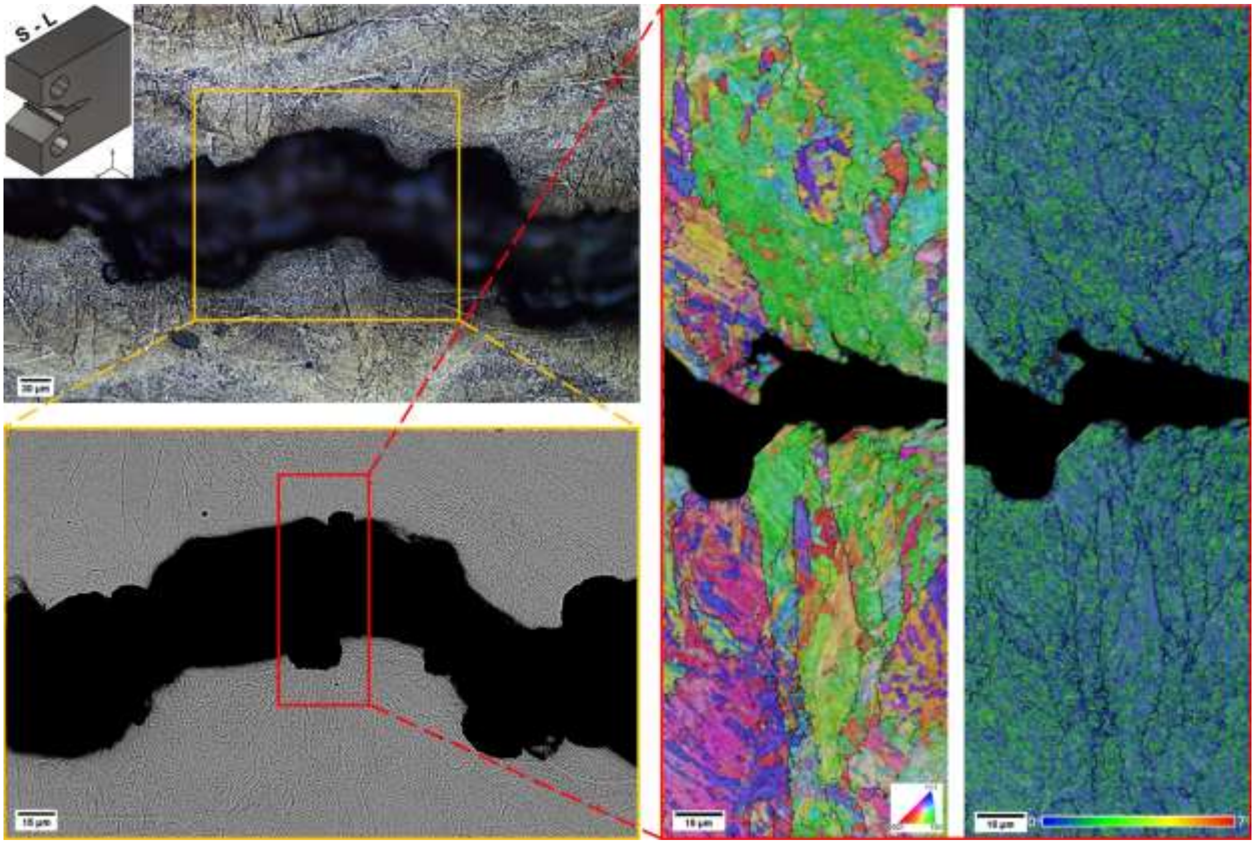

Fig. 12: Microstructural analyses on the vertical cross section of a fractured W-4130 CT specimen in AB condition and tested along S-L orientation.

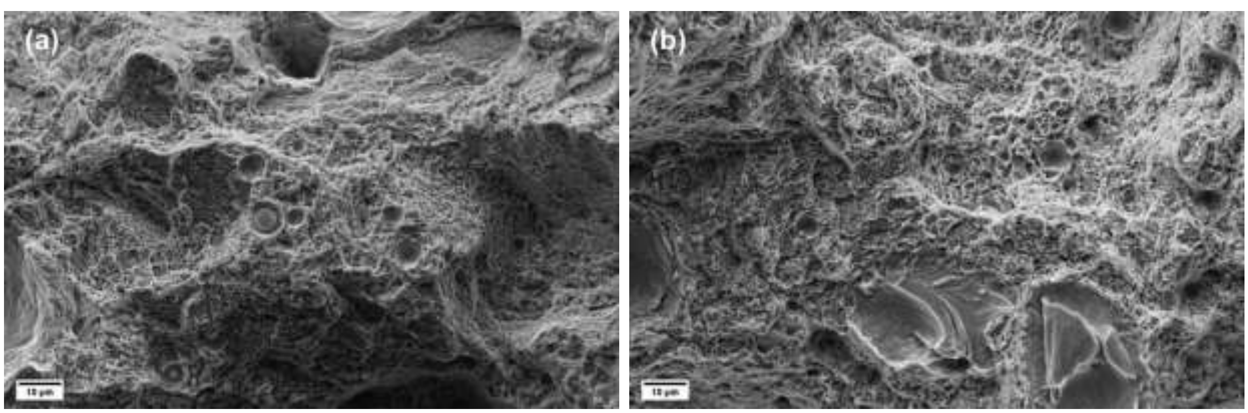

Fig. 13: Fracture surfaces of (a) L-S and (b) S-L W-4130 specimens in as-built condition.

4. Conclusions

The present study focused on the microstructural and fracture behavior of a water atomized 4130 low-alloy steel processed by Laser powder bed fusion starting. The main outcomes are summarized as follows:

- The water atomized feedstock contains a higher level of oxygen than a corresponding gas atomized powder, which leads to a different population of non-metallic inclusions after Laser processing. A reduced hardenability of the water atomized steel was also measured in comparison to the gas atomized counterpart, due to variations in chemical compositions and as a result of the larger presence of SiO_2-type inclusions that could stimulate on cooling the nucleation of other phases rather than martensite.
- Consistently the Charpy-V impact toughness of the Water atomized 4130 steel showed a slight drop over the gas atomized counterpart. Despite the effects induced by the dispersed inclusions, the obtained impact toughness values were comparable to those provided by other L-PBF low-alloy steels published in the literature.
- The fracture toughness behavior suggested an easier condition for crack propagation in a direction orthogonal to the building direction, when considering both as-built and quench and tempered conditions.
- The quench and tempering treatment generated a more homogenous microstructure and significantly enhanced both the tensile fracture elongation and the fracture toughness behavior with respect to as built condition. However, no pronounced improvement was measured in the case of impact toughness property.

Acknowledgements

The investigation was carried out within the frame of the SPAcEMAN project funded by EIT-Raw Materials in 2018-2021. The Italian Ministry of Education, University and Research is also acknowledged for the support provided through the project "Department of Excellence LIS4.0 - Lightweight and Smart Structures for Industry 4.0”. Marawan Abdelwahed was funded by a full Ph.D. scholarship from the Ministry of Higher Education of the Arab Republic of Egypt. The authors would like to express their gratitude to Luca Signorelli, Lorenzo Giudici, Ludovica Rovatti, and Michael Ishola for their collaboration and technical support at Politecnico di Milano.

Data availability

The raw/processed data required to reproduce these findings cannot be shared at this time as the data also forms part of an ongoing study.

References

[1] P. Bajaj, A. Hariharan, A. Kini, P. Kürnsteiner, D. Raabe, E.A. Jägle, Steels in

additive manufacturing: A review of their microstructure and properties, Mater. Sci. Eng. A. 772 (2020) 138633. https://doi.org/10.1016/j.msea.2019.138633.

[2] W. Wang, S. Kelly, A Metallurgical Evaluation of the Powder-Bed Laser Additive Manufactured 4140 Steel Material, JOM. 68 (2016) 869–875. https://doi.org/10.1007/s11837-015-1804-y.

[3] J.J.S. Dilip, G.D.J. Ram, T.L. Starr, B. Stucker, Selective laser melting of HY100 steel: Process parameters, microstructure and mechanical properties, Addit. Manuf. 13 (2017) 49–60. https://doi.org/10.1016/j.addma.2016.11.003.

[4] E. Jelis, M.R. Hespos, N.M. Ravindra, Process Evaluation of AISI 4340 Steel Manufactured by Laser Powder Bed Fusion, J. Mater. Eng. Perform. (2018). https://doi.org/10.1007/s11665-017-2989-8.

[5] L. zhi Wang, J. jiao Wu, X. fei Huang, X. fu Hong, SLM-manufactured 30CrMnSiA alloy: Mechanical properties and microstructural effects of designed heat treatment, Opt. Laser Technol. 107 (2018) 89–98. https://doi.org/10.1016/J.OPTLASTEC.2018.05.020.

[6] M. Wei, S. Chen, L. Xi, J. Liang, C. Liu, Selective laser melting of 24CrNiMo steel for brake disc: Fabrication efficiency, microstructure evolution, and properties, Opt. Laser Technol. 107 (2018) 99–109. https://doi.org/10.1016/J.OPTLASTEC.2018.05.033.

[7] X. Li, Y.H. Tan, H.J. Willy, P. Wang, W. Lu, M. Cagirici, C.Y.A. Ong, T.S. Herng, J. Wei, J. Ding, Heterogeneously tempered martensitic high strength steel by selective laser melting and its micro-lattice: Processing, microstructure, superior performance and mechanisms, Mater. Des. 178 (2019) 107881. https://doi.org/10.1016/J.MATDES.2019.107881.

[8] J. Damon, R. Koch, D. Kaiser, G. Graf, S. Dietrich, V. Schulze, Process development and impact of intrinsic heat treatment on the mechanical performance of selective laser melted AISI 4140, Addit. Manuf. 28 (2019) 275–284. https://doi.org/10.1016/j.addma.2019.05.012.

[9] M. Abdelwahed, R. Casati, S. Bengtsson, A. Larsson, M. Riccio, M. Vedani, Effects of Powder Atomisation on Microstructural and Mechanical Behaviour of L-PBF Processed Steels, Metals (Basel). 10 (2020) 1474. https://doi.org/10.3390/met10111474.

[10] L. Zumofen, A. Kirchheim, H.-J. Dennig, Laser powder bed fusion of 30CrNiMo8 steel for quenching and tempering: examination of the processability and mechanical properties, Prog. Addit. Manuf. 5 (2020) 75–81. https://doi.org/10.1007/s40964-020-00121-x.

[11] R. Seede, D. Shoukr, B. Zhang, A. Whitt, S. Gibbons, P. Flater, A. Elwany, R. Arroyave, I. Karaman, An ultra-high strength martensitic steel fabricated using selective laser melting additive manufacturing: Densification, microstructure, and mechanical properties, Acta Mater. 186 (2020) 199–214. https://doi.org/10.1016/J.ACTAMAT.2019.12.037.

[12] Y.R. Han, C.H. Zhang, X. Cui, S. Zhang, J.B. Zhang, Y. Liu, The formability and microstructure evolution of 24CrNiMo alloy steel fabricated by selective laser melting, Vacuum. 175 (2020) 109297. https://doi.org/10.1016/j.vacuum.2020.109297.

[13] M. Abdelwahed, S. Bengtsson, R. Casati, A. Larsson, S. Petrella, M. Vedani, Effect

of water atomization on properties of type 4130 steel processed by L-PBF, Mater. Des. 210 (2021) 110085. https://doi.org/10.1016/j.matdes.2021.110085.

[14] T.H. Becker, P. Kumar, U. Ramamurty, Fracture and fatigue in additively manufactured metals, Acta Mater. 219 (2021) 117240. https://doi.org/10.1016/j.actamat.2021.117240.

[15] J. Suryawanshi, K.G. Prashanth, U. Ramamurty, Mechanical behavior of selective laser melted 316L stainless steel, Mater. Sci. Eng. A. 696 (2017) 113–121. https://doi.org/10.1016/J.MSEA.2017.04.058.

[16] J. Suryawanshi, K.G. Prashanth, U. Ramamurty, Tensile, fracture, and fatigue crack growth properties of a 3D printed maraging steel through selective laser melting, J. Alloys Compd. 725 (2017) 355–364. https://doi.org/10.1016/j.jallcom.2017.07.177.

[17] J. Maciejewski, The Effects of Sulfide Inclusions on Mechanical Properties and Failures of Steel Components, J. Fail. Anal. Prev. 15 (2015). https://doi.org/10.1007/s11668-015-9940-9.

[18] R. Vaz Penna, L.N. Bartlett, T. Constance, Understanding the Role of Inclusions on the Dynamic Fracture Toughness of High Strength Lightweight FeMnAl Steels, Int. J. Met. 13 (2019) 286–299. https://doi.org/10.1007/s40962-018-0273-9.

[19] X. Lou, P.L. Andresen, R.B. Rebak, Oxide inclusions in laser additive manufactured stainless steel and their effects on impact toughness and stress corrosion cracking behavior, J. Nucl. Mater. (2018). https://doi.org/10.1016/j.jnucmat.2017.11.036.

[20] D.F. Heaney, Powders for metal injection molding (MIM), in: Handb. Met. Inject. Molding, Elsevier, 2012: pp. 50–63. https://doi.org/10.1533/9780857096234.1.50.

[21] S. Cacace, Q. Semeraro, Influence of the atomization medium on the properties of stainless steel SLM parts, Addit. Manuf. 36 (2020) 101509. https://doi.org/10.1016/j.addma.2020.101509.

[22] M. Abdelwahed, S. Bengsston, R. Casati, A. Larsson, M. Vedani, L-PBF Processing of Steel Powders Produced by Gas and Water Atomization, BHM Berg- Und Hüttenmännische Monatshefte. 166 (2021) 40–45. https://doi.org/10.1007/s00501-020-01071-1.

[23] M. Abdelwahed, R. Casati, A. Larsson, S. Petrella, S. Bengtsson, M. Vedani, On the Recycling of Water Atomized Powder and the Effects on Properties of L-PBF Processed 4130 Low-Alloy Steel, Materials (Basel). 15 (2022) 336. https://doi.org/10.3390/ma15010336.

[24] R. Seede, B. Zhang, A. Whitt, S. Picak, S. Gibbons, P. Flater, A. Elwany, R. Arroyave, I. Karaman, Effect of heat treatments on the microstructure and mechanical properties of an ultra-high strength martensitic steel fabricated via laser powder bed fusion additive manufacturing, Addit. Manuf. 47 (2021) 102255. https://doi.org/10.1016/J.ADDMA.2021.102255.

[25] E. Jelis, M. Clemente, S. Kerwien, N.M. Ravindra, M.R. Hespos, Metallurgical and Mechanical Evaluation of 4340 Steel Produced by Direct Metal Laser Sintering, JOM. 67 (2015) 582–589. https://doi.org/10.1007/s11837-014-1273-8.

[26] T. Nakamoto, N. Shirakawa, Y. Miyata, H. Inui, Selective laser sintering of high carbon steel powders studied as a function of carbon content, J. Mater. Process. Technol. 209 (2009) 5653–5660. https://doi.org/10.1016/J.JMATPROTEC.2009.05.022.

[27] E.N. DIN, 10083-3 (2007) Steels for quenching and tempering-Part 3: Technical delivery conditions for alloy steels, English version, of DIN EN 10083-3: 2007-01, Deutsches Institut für Normung e, V., Berlin. (n.d.). http://www.skl.by/files/information/flat/EN10083-3.pdf

[28] Y. Wang, J. Hua, M. Kong, Y. Zeng, J. Liu, Z. Liu, Quantitative analysis of martensite and bainite microstructures using electron backscatter diffraction, Microsc. Res. Tech. 79 (2016) 814–819. https://doi.org/10.1002/jemt.22703.

[29] M.-S. Baek, K.-S. Kim, T.-W. Park, J. Ham, K.-A. Lee, Quantitative phase analysis of martensite-bainite steel using EBSD and its microstructure, tensile and high-cycle fatigue behaviors, Mater. Sci. Eng. A. 785 (2020) 139375. https://doi.org/10.1016/j.msea.2020.139375.

[30] H. Chen, D. Gu, D. Dai, C. Ma, M. Xia, Microstructure and composition homogeneity, tensile property, and underlying thermal physical mechanism of selective laser melting tool steel parts, Mater. Sci. Eng. A. 682 (2017) 279–289. https://doi.org/10.1016/j.msea.2016.11.047.

[31] P.P. Suikkanen, C. Cayron, A.J. DeArdo, L.P. Karjalainen, Crystallographic Analysis of Martensite in 0.2C-2.0Mn-1.5Si-0.6Cr Steel using EBSD, J. Mater. Sci. Technol. 27 (2011) 920–930. https://doi.org/10.1016/S1005-0302(11)60165-5.

[32] J.C.F. Jorge, L.F.G.D. Souza, M.C. Mendes, I.S. Bott, L.S. Araújo, V.R.D. Santos, J.M.A. Rebello, G.M. Evans, Microstructure characterization and its relationship with impact toughness of C–Mn and high strength low alloy steel weld metals – a review, J. Mater. Res. Technol. 10 (2021) 471–501. https://doi.org/10.1016/J.JMRT.2020.12.006.

[33] T. Tsuchiyama, M. Natori, N. Nakada, S. Takaki, Conditions for grain boundary bulging during tempering of lath martensite in ultra-low carbon steel, ISIJ Int. 50 (2010). https://doi.org/10.2355/isijinternational.50.771.

[34] M. Salandre, S. Garabedian, G. Gaillard, T. Williamson, T. Joffre, Development of a New Tooling Steel (L40) for Laser Powder Bed Fusion: Influence of Particle Size Distribution and Powder Atomization on Mechanical Performance, Adv. Eng. Mater. 23 (2021). https://doi.org/10.1002/adem.202100350.